The Cryosphere Discuss., 7, 1907–1925, 2013
www.the-cryosphere-discuss.net/7/1907/2013/
doi:10.5194/tcd-7-1907-2013

The Cryosphere Discussions
Open Access

Weak layer fracture: facets and depth hoar

I. Reiweger and J. Schweizer

WSL Institute for Snow and Avalanche Research SLF, Davos, Switzerland

Received: 22 April 2013 – Accepted: 22 April 2013 – Published: 3 May 2013

Correspondence to: I. Reiweger (reiweger@slf.ch)

Published by Copernicus Publications on behalf of the European Geosciences Union.

Abstract

Understanding the fracture behavior of weak snow layers is essential for modeling and predicting dry-snow slab avalanches. We therefore performed laboratory experiments with snow samples containing a weak layer consisting of either faceted crystals or depth hoar. During these experiments the samples were loaded with different loading rates and at various tilt angles until fracture. The strength of the samples decreased with increasing loading rate and increasing tilt angle. Additionally, we took pictures of the side of the samples with a high-speed video camera and calculated the displacement using a particle image velocimetry (PIV) algorithm. The fracture process within the weak layer could thus be studied in detail. We found a fracture in shear immediately followed by a collapse of the weak layer.

1 Introduction

Most skier-triggered dry-snow slab avalanches release due to the failure of a weak layer consisting of depth hoar, faceted crystals, or surface hoar crystals (Schweizer and Jamieson, 2001). A macroscopic crack ($\mathcal{O}$(10 cm) or more) in the weak layer underlying a cohesive slab might lead to crack propagation and eventually to the release of a slab avalanche (Schweizer et al., 2003). The initial failure and its extension to the critical crack size leading to fast crack propagation is still not fully understood.

Heierli et al. (2008) suggested avalanche initiation to be modeled as a mixed-mode anticrack where the main mechanism behind weak layer failure is collapse of the weak layer. Other authors such as McClung (1979, 2009) or Bažant et al. (2003) suggest that the layer first fails in shear.

Previous laboratory studies on the mechanical behavior of snow mainly used displacement-controlled shear experiments. Most experiments were made with homogeneous snow (e.g. McClung, 1977; de Montmollin, 1982; Schweizer, 1998). Those studies showed that snow is a pressure sensitive and strain-softening material, the latter

TCD
7, 1907–1925, 2013

was assumed to be a consequence of sintering processes inside the snow during deformation (e.g. Colbeck, 1998; Reiweger et al., 2009b). In addition, it was shown that snow strength decreases with increasing rate of displacement (Narita, 1980).

Weak snow layers were tested in the field (Föhn et al., 1998; Jamieson and Johnston, 2001) as well as in the laboratory (Fukuzawa and Narita, 1993; Joshi et al., 2006; Reiweger and Schweizer, 2010; Walters et al., 2010; Walters and Adams, 2012). The laboratory studies showed that the deformation subjected to a snow samples was concentrated in the weak layer, which provides a preferential plane for shear failure. In the experiments we performed with samples containing a weak layer of surface hoar (Reiweger and Schweizer, 2010) we found that at least this kind of weak layer failed in shear more likely than in compression.

We performed loading experiments with snow samples containing a weak depth hoar layer with a new loading apparatus especially designed for studying the failure of snow with respect to avalanche release. In order to obtain loading conditions similar to those in nature, the samples were loaded by a combination of shear and normal load depending on the tilt angle. A detailed description of our loading apparatus is given in Reiweger et al. (2010).

2 Methods

2.1 Snow samples and loading experiments

The snow samples containing a weak layer were either artificial samples (samples TRA and LAY, Table 1) produced in the laboratory (Reiweger et al., 2010) or natural samples taken from the field (samples B, Table 1). The layering of the samples is shown in Table 1. The weak layer in the artificial samples was a thin layer of faceted crystals, whereas the natural samples contained a thick weak layer of large depth hoar crystals.

The loading experiments were performed at a temperature of −5 °C with the apparatus shown in Figure 1 and described by Reiweger et al. (2010). Loading rates varied

TCD
7, 1907–1925, 2013

between 10 Pa s^{-1} and 400 Pa s^{-1}. Samples were tilted (0–35°) in order to mimic a "slope angle" and loaded via the gravitational force. The weight of the upper sample holder was compensated.

2.2 Particle image velocimetry

In order to monitor the displacement field on the sides of our samples we took photos during the measurements. These photos were then analyzed with a particle image velocimetry algorithm (PIV). Assuming plane strain conditions, the displacement field on the side of the sample should be representative for the displacement field also within the sample. A detailed description of the PIV algorithm can be found in Roesgen and Totaro (1995); its application to snow is described in Reiweger et al. (2009a); van Herwijnen (2013). For the fast experiments with samples B8, B9, B10, and B17, we acquired images at a high rate with a high-speed video camera (camera type VDS Vosskühler HCC-1000, resolution 1024 by 512 pixels, recording rate 300 frames per second). Since the weak layer B was several centimeters thick we could observe what was happening within the weak layer shortly before and during fracture.

3 Results

3.1 Strength

We performed 29 experiments with three sample types for various loading rates. Detailed results of all measurements can be found in Table 2.

Figure 2 shows the strength for samples of types TRA and LAY as function of tilt angle and loading rate. Due to the limited number of experiments for each loading rate and tilt angle, we calculated the standard deviation with a bootstrap algorithm (Davison and Hinkley, 1997), using 2000 sample data sets. It can be see that strength decreases

TCD
7, 1907–1925, 2013

with increasing tilt angle and increasing loading rate. For samples TRA and LAY both these trends are clearly larger than the standard deviation.

For samples of type B (Fig. 3) the decrease of strength with increasing tilt angle and loading rate is still apparent – as the highest strength values are clearly found at a tilt angle of 0° – but not as obvious, since the strength differences between 25° and 35° are of the same order of magnitude as the standard deviation (again calculated with the bootstrap algorithm). Comparing the measurements below and above a loading rate of 150 Pa s^{-1}, however, the decrease with strength with increasing loading rate remains evident.

3.2 Fracture behavior

The fracture of samples B8, B9, B10, and B17 was monitored with a high-speed video camera. The images from the high-speed videos were again analyzed with the particle image velocimetry (PIV) algorithm. Detailed results are given for sample B9, which was loaded with a loading rate of 18 Pa s^{-1} at a tilt angle of 35° (Tab. 2).

For the PIV analysis we chose two different sections of the snow sample, i.e. an upper rectangle (dimensions 22 mm × 87 mm, Fig. 4a) where a local fracture happened and a lower rectangle (dimensions 16 mm × 64 mm, Fig. 4b) where the catastrophic fracture of the whole sample commenced. The arrows in Figure 4 mark those two fracture locations. The weak layer is approximately located between the two red lines (Fig. 4a). Analysis of the 33 images before and after the onset of the final crack allowed us to exactly follow the fracture process. The PIV results show the displacement between the first of the 33 images and image i, where $i = 2, \ldots, 33$. The time difference between two subsequent images was 1/300 s, and the displacement was averaged across the width of the rectangles shown in Fig. 4. The first series of PIV results shown in Fig. 5 shows the displacement caused by the local fracture within the upper rectangle (Fig. 4a). The parallel arrows in the middle of the displacement fields indicate that the catastrophic failure has started, as the snow starts moving to the right and downwards as a cohesive block (Fig. 7a). The seemingly chaotic and even upward

TCD
7, 1907–1925, 2013

movement during fracture (Fig. 5) reflects the layer being crushed and pieces of snow being pressed out of the sample sideways. The second series of images (Fig. 6) shows the PIV results of the onset of the final crack within the lower rectangle (Fig. 4b). At image 29 we see the onset of the catastrophic shear fracture, the upper arrows pointing forward, the lower arrows pointing backward. The image of sample B9 0.3 s after the image shown in Fig. 4 (which were taken 0.01 s before the first local failure at the top of the sample appeared) is displayed in Fig. 7b. The upper and lower parts of the sample are still fairly intact, but the weak layer is squashed and the snow has crumbled away sideways. The final image of the high speed camera sequence (Fig. 7c), taken 1 s after the images in Fig. 4, shows the sample holders after the samples has fractured catastrophically. The movies taken during the experiments with samples B8, B10, and B17 showed similar behavior.

4 Discussion

When testing samples including a weak layer the sample geometry and loading conditions are often not perfect. Natural depth hoar samples are especially difficult to harvest, since, in contrast to layers of buried surface hoar, they are usually at the bottom of the snowpack and hardly ever have a cohesive layer beneath them. In the case of samples of kind B, we were lucky to have a crust below the depth hoar layer, which made it possible to cut and transport samples. The height of the samples had to be chosen quite large for the reason of keeping the crust at the bottom. We are aware that this gives an unfavorable area to height ratio for the whole sample. Studying the deformation during the experiment, though, we see a concentration of deformation at the interface between the weak layer and the crust below. This is also the location where the samples fractured. Considering this very thin weak interface, the area to height ratio seems acceptable.

The artificial samples had a thin weak layer, which improved the area to height ratio, especially since for layered samples the deformation is concentrated within the weak

TCD
7, 1907–1925, 2013

layer (Reiweger et al., 2009a; Reiweger and Schweizer, 2010). For the artificial samples TRA and LAY we found a strong decrease of sample strength with increasing tilt angle, suggesting a failure in shear rather than in compression. The measurements with the natural samples B showed this trend as well, though less prominent. We assume that this is due to the height of the samples, which was unfavorably high compared to the sample area, as discussed above.

The well known (Fukuzawa and Narita, 1993; Schweizer, 1998) rate dependence of snow strength was reproduced well for all our samples, i.e. sample strength decreased with increasing loading rate. The absolute strength of the samples might be higher than the strength of a similar weak layer in a natural snowpack due to the finite size of the (relatively small) samples (Bažant et al., 2004). The tendency, i.e. the strength decrease, should not be affected by size effect, however, and can therefore be assumed to be valid also for natural weak layers in the field.

The high-speed video images from the fracture of samples B9 show that a small fracture occurred at an arbitrary place within the weak layer, and this fracture then triggered a shear crack at the interface between the weak layer and the crust at the bottom. This crack propagated through the whole sample (in x-direction, Fig. 1) and caused the sample to fail catastrophically. A similar fracture mechanism was observed for all four samples which were filmed with the high-speed camera. However, these observations might be specific to our thick samples of natural depth hoar.

The movies from samples B8, B9, B10, and B17 are unique in showing the actual formation of the catastrophic fracture of a weak depth hoar layer. All four movies suggest that the fracture started as a shear fracture (Fig. 6, image 29) at the interface of the depth hoar layer and the crust below the layer. This catastrophic failure was triggered by some disturbance somewhere within the weak layer, maybe at a point where the weak layer had a particularly weak spot due to the inherent small-scale inhomogeneity of snow layers. During fracture the samples then collapsed completely (Fig. 7).

TCD
7, 1907–1925, 2013

5 Conclusions

We performed 29 loading experiments with samples containing a weak layer of either facets or depth hoar. Strength decreased with increasing loading rate and tilt angle. The decrease in strength with increasing tilt angle suggests that facets and depth hoar are more prone to failure in shear than to failure in compression, as was previously shown for samples containing a weak layer of surface hoar (Reiweger and Schweizer, 2010). The collapse of the whole weak layer seems to be a consequence of the failure in shear, not vice versa. For natural avalanche release this means that steep terrain favors the initiation of a crack.

During the experiments with the thick depth hoar samples we could actually follow how the initial failure started. It seemed to start as a local failure at a seemingly arbitrary position within the weak layer which induced a shear crack at the weak interface between the depth hoar layer and the crust below. So the inherent disordered nature of snow seems to be important for failure initiation, and a weak layer or weak interface is needed where a macroscopic crack which can grow large enough for crack propagation can form.

Supplementary material related to this article is available online at: http://www.the-cryosphere-discuss.net/7/1907/2013/tcd-7-1907-2013-supplement.zip.

Acknowledgements. We thank Stephan Simioni, Susanna Hoinkes, and Klemens Mayer for help with the experiments.

References

Bažant, Z., Zi, G., and McClung, D.: Size effect law and fracture mechanics of the triggering of dry snow slab avalanches, J. Geophys. Res., 108, doi:10.1029/2002JB001884, 2003.

Bažant, Z., Pang, S., Vořechovskỳ, M., Novák, D., and Pukl, R.: Statistical size effect in quasibrittle materials: Computation and extreme value theory, in: 5th International Conference FraMCoS- Fracture Mechanics of Concrete and Structures, Vail, Colorado, USA, 189–196, 2004.
Colbeck, S.: Sintering in a dry snow cover, J. Appl. Phys., 84, p. 4585, 1998.
Davison, A. and Hinkley, D.: Bootstrap Methods and Their Application, Cambridge University Press, Cambridge, 1997.
de Montmollin, V.: Shear tests on snow explained by fast metamorphism, J. Glaciol., 28, 187–198, 1982.
Fierz, C., Armstrong, R., Durand, Y., Etchevers, P., Greene, E., McClung, D., Nishimura, K., Satyawali, P., and Sokratov, S.: The International Classification for Seasonal Snow on the Ground., Paris, UNESCO-International Hydrological Program, (IHP-VII Technical Documents in Hydrology), 83, 90 pp., 2009.
Föhn, P., Camponovo, C., and Krüsi, G.: Mechanical and structural properties of weak snow layers measured in situ, Ann. Glaciol., 26, 1–6, 1998.
Fukuzawa, T. and Narita, H.: An experimental study on the mechanical behavior of a depth hoar layer under shear stress, in: Proceedings International Snow Science Workshop, 4–8 October 1992, Breckenridge, Colorado, USA, 171–175, 1993.
Heierli, J., Gumbsch, P., and Zaiser, M.: Anticrack nucleation as triggering mechanism for snow slab avalanches, Science, 321, 240–243, 2008.
Jamieson, J. B. and Johnston, C. D.: Evaluation of the shear frame test for weak snowpack layers, Ann. Glaciol., 32, 59–69, 2001.
Joshi, S. K., Mahajan, P., and Upadhyay, A.: Study of Layered Snow under Shear and Tension, in: Proceedings ISSW 2006. International Snow Science Workshop, edited by Gleason, A., 1–6 October 2006, Telluride, Colorado, USA, 165–173, 2006.
McClung, D.: Direct simple shear tests on snow and their relation to slab avalanche formation, J. Glaciol., 19, 101–109, 1977.
McClung, D.: Shear fracture precipated by strain-softening as a mechnism of dry slab avalanche release, J. Geophys. Res., 84, 3519–3526, 1979.
McClung, D.: Dry snow slab quasi-brittle fracture initiation and verification from field tests, J. Geophys. Res., 114, F01022, 2009.
Narita, H.: Mechanical behaviour and structure of snow under uniaxial tensile stress, J. Glaciol., 26, 275–282, 1980.

TCD
7, 1907–1925, 2013

Reiweger, I. and Schweizer, J.: Failure of a layer of buried surface hoar, Geophys. Res. Lett., 37, L24501, 2010.
Reiweger, I., Ernst, R., Schweizer, J., and Dual, J.: Force-controlled shear experiments with snow samples, in: Proceedings International Snow Science Workshop, 7 September–2 October 2009, edited by: Schweizer, J. and van Herwijnen, A., Davos, Switzerland, 2, 120–123, 2009a.
Reiweger, I., Schweizer, J., Dual, J., and Herrmann, H.: Modelling snow failure with a fibre bundle model, J. Glaciol., 55, 997–1002, 2009b.
Reiweger, I., Schweizer, J., Ernst, R., and Dual, J.: Load-controlled test apparatus for snow, Cold Reg. Sci. Technol., 62, 119–125, 2010.
Roesgen, T. and Totaro, R.: Two-dimensional on-line particle imaging velocimetry, Experiments in Fluids, 19, 188–193, 1995.
Schweizer, J.: Laboratory experiments on shear failure of snow, Ann. Glaciol., 26, 97–102, 1998.
Schweizer, J. and Jamieson, J. B.: Snow cover properties for skier triggering of avalanches, Cold Reg. Sci. Technol., 33, 207–221, 2001.
Schweizer, J., Jamieson, J. B., and Schneebeli, M.: Snow avalanche formation, Rev. Geophys., 41, 1016, 2003.
van Herwijnen, A.: Experimental analysis of SMP cone penetration in homogeneous snow layers, Canadian Geo. J., submitted, 2013.
Walters, D. J. and Adams, E. E.: Directional mechanical properties of radiation recrystallized snow layers from experimental testing, in: Proceedings International Snow Science Workshop, 16–21 September 2012, edited by: Johnson, J. and Conway, H., Anchorage, Alaska, USA, 201–208, 2012.
Walters, D. J., Adams, E. E., Staron, P. J., and McKittrick, L. R.: Shear deformation of radiation recrystallized near surface facets, in: Proceedings International Snow Science Workshop, 17–22 October 2010, edited by: Osterhuber, R., Lake Tahoe, CA, USA, 80–87, 2010.

TCD
7, 1907–1925, 2013

Table 1. Characteristics of the different snow samples tested. Snow type is described as grain type according to Fierz et al. (2009), average grain size (in mm), and hand hardness index, while *N* denotes the number of successful experiments performed with each type of sample.

Sample layering	Density ($kg\,m^{-3}$)	Thickness (mm)	Length × Width (mm)	Snow type	*N*
rounded grains depth hoar TRA rounded grains	225	35 0.2 40	120 × 90	RG, 0.25, 1-2 FC(DH), 1-1.5, 1 RG, 0.25, 1-2	8
rounded grains faceted crystals LAY rounded grains	190	35 0.2 35	120 × 90	RG, 0.5, 2 FC(FCxr), 0.75, 1 RG, 0.5, 2	4
rounded grains depth hoar B melt-freeze crust	200	40 50 20	200 × 100	RG(FC), 0.25-1.5, 2-3 DH(FC), 1.25-3, 1 MFcr, 1-2, 4	17

TCD
7, 1907–1925, 2013

Table 2. Overview of all successful measurements. α, $\dot{\sigma}$, and σ_c denote the slope angle, the loading rate, and the sample strength, respectively.

Sample	α (°)	$\dot{\sigma}$ (Pa s^{-1})	σ_c (kPa)
TRA1	20	60	2.1
TRA2	20	150	1.9
TRA3	30	60	0.5
TRA4	30	60	0.8
TRA5	20	60	2.1
TRA6	20	150	1.1
TRA7	20	150	2.4
TRA8	20	150	1.5
LAY1	10	150	2.5
LAY2	10	60	5.3
LAY3	10	150	2.6
LAY4	10	60	> 10
B1	25	42	1.6
B2	25	200	0.7
B3	25	84	2.4
B4	25	9	2.3
B5	25	14	2.0
B6	35	10	3.8
B7	35	200	1.0
B8	35	200	1.2
B9	35	18	1.7
B10	35	20	0.8
B11	0	444	2.7
B12	0	439	2.5
B13	0	30	2.5
B14	0	15	2.5
B15	25	290	1.3
B16	0	42	6.0
B17	25	220	1.7

TCD
7, 1907–1925, 2013

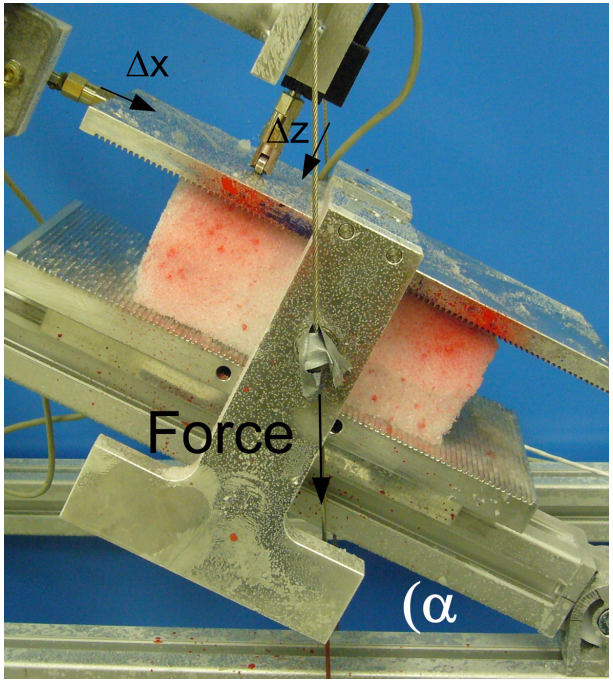

Fig. 1. Snow sample in loading apparatus. Δx and Δz denote the shear and normal displacement, α denotes the tilt angle (Reiweger et al., 2010).

TCD
7, 1907–1925, 2013

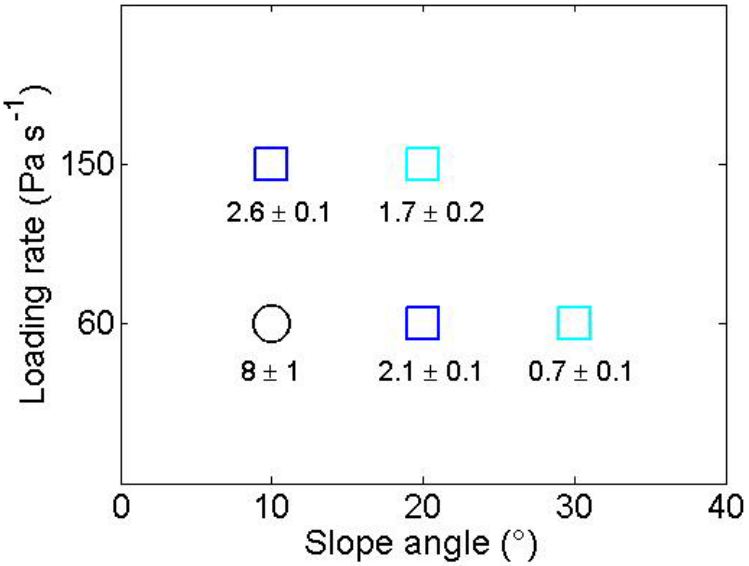

Fig. 2. Strength σ_c in kPa for samples TRA and LAY as function of slope angle and loading rate (N = 12). The colors illustrate the order of magnitude of sample strength, squares indicate fracture, the circle indicates that one sample did not fracture at this tilt angle and loading rate.

TCD
7, 1907–1925, 2013

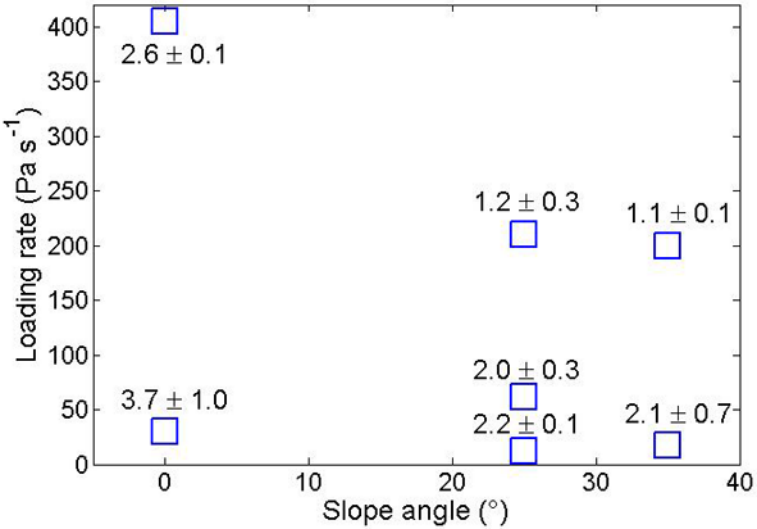

Fig. 3. Strength σ_c in kPa for samples of type B as function of tilt angle and loading rate (N = 17).

TCD
7, 1907–1925, 2013

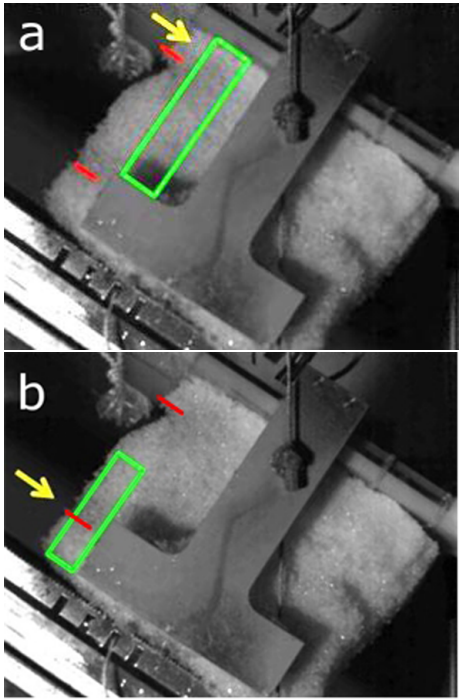

Fig. 4. (a) Section (green rectangle) where first local failure occurred. **(b)** Section where the crack propagation started. The red lines mark the position of the weak layer. Sample B9.

TCD
7, 1907–1925, 2013

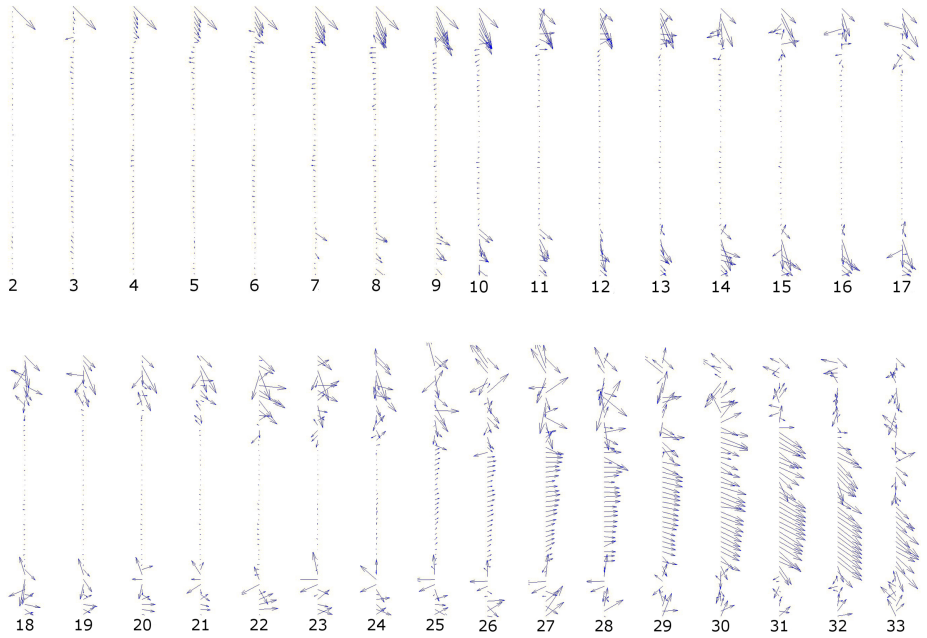

Fig. 5. Horizontally averaged displacement field within the upper rectangle (Fig. 4a) during the failure process of sample B9. The displacement is shown between image 1 and images 2–33, respectively. The uppermost arrow in each sequence is only for reference, its coordinates are [0.8 mm, 0.8 mm]. The time difference between subsequent images was 1/300 s.

TCD
7, 1907–1925, 2013

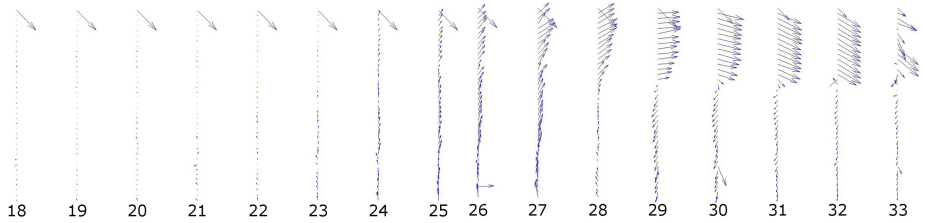

Fig. 6. Averaged displacement field within the lower rectangle during the initiation of the catastrophic fracture(Fig. 4b) of sample B9. Displacement is shown between image 1 and images 18–33. Again uppermost arrow for reference, coordinates [0.8 mm, 0.8 mm] (same as in Fig. 5).

TCD
7, 1907–1925, 2013

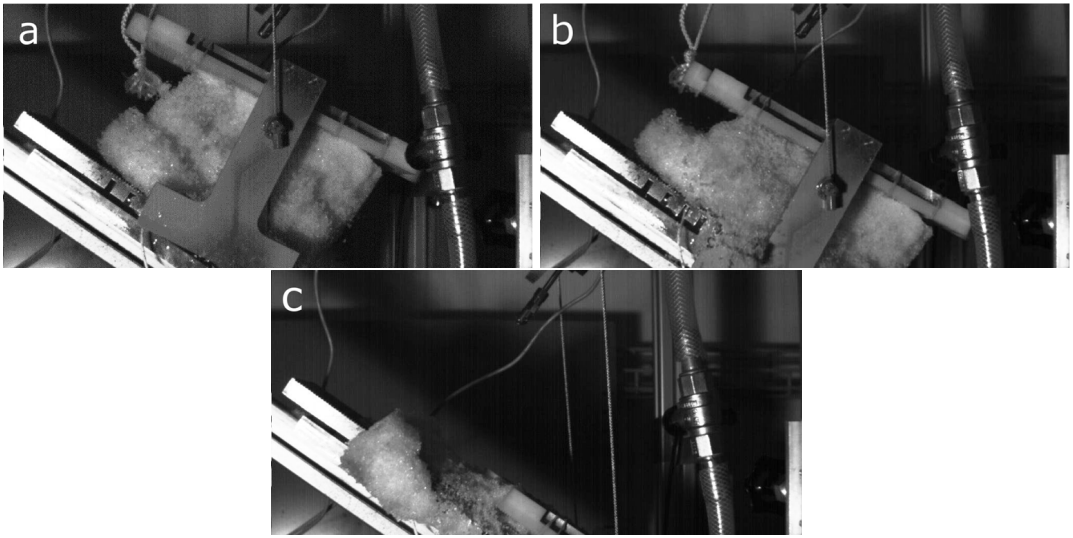

Fig. 7. Sample B9, during catastrophic failure. The images **(b)** and **(c)** were taken 0.1 s and 0.9 s after image **(a)**, respectively.

TCD
7, 1907–1925, 2013